Acta Oceanol. Sin., 2024, Vol. 43, No. 4, P. 25–39
https://doi.org/10.1007/s13131-024-2337-4
http://www.aosocean.com
E-mail: ocean2@hyxb.org.cn

Geometry and 3D seismic characterisation of post-rift normal faults in the Pearl River Mouth Basin, northern South China Sea

Yuanhang Liu[1, 2], Jinwei Gao[1, 2*], Wanli Chen[1], Jiliang Wang[1], Umair Khan[1]

[1] Laboratory of Marine Geophysics and Georesources, Institute of Deep-sea Science and Engineering, Chinese Academy of Sciences, Sanya 572000, China

[2] University of Chinese Academy of Sciences, Beijing 100049, China

Received 31 July 2023; accepted 27 December 2023

Abstract

Based on high-resolution 3D seismic data acquired in the Pearl (Zhujiang) River Mouth Basin of the northern South China Sea, this study investigated the geometry, spatial extension, and throw distribution of the post-rift normal fault through detailed seismic interpretation and fault modeling. A total of 289 post-rift normal faults were identified in the study area and can be classified into four types: (1) isolated normal faults above the carbonate platform; (2) isolated normal faults cutting through the carbonate platform; (3) conjugate normal faults, and (4) connecting normal faults. Throw distribution analysis on the fault planes show that the vertical throw profiles of most normal fault exhibit flat-topped profiles. Isolated normal faults above the carbonate platform exhibit roughly concentric ellipses with maximum throw zones in the central section whereas the normal faults cutting through the carbonate platform miss the lowermost section due to the chaotic seismic reflections in the interior of the carbonate platform. The vertical throws of conjugate normal faults anomalously decrease toward their intersection region on the fault plane whereas the connecting normal faults present two maximum throw zones in the central section of the fault plane. According to the symmetric elliptical distribution model of fault throw, an estimation was made indicating that normal faults cutting through the carbonate platform extended downward between –1 308 s and –1 780 s (two-way travel time) in depth and may not penetrate the entire Liuhua carbonate platform. Moreover, it is observed that the distribution of karst caves on the top of the carbonate platform disaccord with those of hydrocarbon reservoirs and the post-rift normal faults cutting through the carbonate platform in the study area. We propose that these karst caves formed most probably by corrosive fluids derived from magmatic activities during the Dongsha event, rather than pore waters or hydrocarbons.

Key words: Post-rift normal faults, fault throw, Karst caves, Corrosive fluids, Pearl River Mouth Basin, South China Sea

Citation: Liu Yuanhang, Gao Jinwei, Chen Wanli, Wang Jiliang, Khan Umair. 2024. Geometry and 3D seismic characterisation of post-rift normal faults in the Pearl River Mouth Basin, northern South China Sea. Acta Oceanologica Sinica, 43(4): 25–39, doi: 10.1007/s13131-024-2337-4

1 Introduction

Analyzing the geometry and displacement distribution of normal faults is helpful for understanding their nucleation and development processes (Hull, 1988; Walsh and Watterson, 1989). The sizes of fault displacements also affect the sealing capacity and permeability of faults, which play an important role in hydrocarbon accumulation and evaluation (Aydin, 2000; Færseth et al., 2007; Song et al., 2022). Early studies found that the displacement on the fault plane of a single normal fault gradually decreases from the maximum value at the center to zero at the fault tips, roughly forming a concentric ellipse (Rippon, 1984; Walsh and Watterson, 1987, 1988). An ideal elliptical model of normal fault throw distribution was proposed and has been used to reveal the relationships of fault throw with the extension on the map view (Watterson, 1986; Walsh and Watterson, 1987, 1988; Barnett et al., 1987; Trudgill et al., 1994; Willemse et al., 1996; Walsh et al., 2003; Kim and Sanderson, 2005; Wibberley et al., 2008), the fault fragmented zone (Knott et al., 1996; Shipton and Cowie, 2001; Fossen, 2016), and the shear modulus (Walsh and Watterson, 1989), in order to analyze fault displacement accumulation process and to predict the geometric structure of faults (Nicol et al., 2017). Subsequently, improved models were proposed to study the differential increasing distribution of fault throw in the process of fault linkage (Peacock and Sanderson, 1991), and to divide the growth stages of idealized extensional fault arrays by analyzing the cumulative fault throw and displacement distribution changes during fault growth (Kim et al., 1994; Cowie et al., 2001; Palumbo et al., 2004; Roberts et al., 2004; Davis et al., 2005; Jackson et al., 2017; Rotevatn et al., 2019).

In recent years, the displacement distribution and growth activity of normal faults have been widely concerned in the northern South China Sea (SCS) in recent years. Huang et al. (2018) studied the growth stage and active characteristics of the normal oblique-slip faults at the Enping Sag in the Pearl River (Zhujiang) Mouth Basin (PRMB) by using the fault displacement

Foundation item: The National Natural Science Foundation of China under contract No. 42276066; the Key Research and Development Program (International Science and Technology Cooperation Development Program) of Hainan Province under contract No. GHYF2022009; the Youth Innovation Promotion Association of CAS under contract No. 2018401.
*Corresponding author, E-mail: gaojw@idsse.ac.cn

distribution along the strike and expansion index (EI). Hu et al. (2021) studied the two-dimensional (2D) geometry and kinematics of the basin-controlling faults in the Qiongdongnan Basin using the throw-depth (T-z) plots and EI. Dai et al. (2022) used the EI and 2D seismic interpretation to analyze the growth and linkage of the main-controlling faults at the Lufeng Sag in the PRMB and provided a three-dimensional (3D) temporal-spatial evolution process of the normal fault system. However, few studies focused on the 3D spatial characteristics and displacement distribution on the fault plane of normal faults in the SCS. Particularly, it is very indistinct for the displacement distribution regularity on the fault plane of the post-rift normal faults in the SCS, which heavily hinders the assessment of post-rift carbonate reservoir properties in the northern SCS.

Post-rift carbonate reservoirs in the Liuhua 11-1 oilfield, situated in the PRMB, represent a significant development and constitute the largest offshore oilfield in China (Sun et al., 2013). Abundant karst caves were observed at the top of the carbonate platform (Sun et al., 2013; Chen et al., 2015). However, controversy exists surrounding the processes governing the formation of these karst caves. Sun et al. (2013) suggested that they caves resulted from corrosive fluids originating from magmatically hydrothermal activity and oil/gas, while Chen et al. (2015) proposed that they were formed by corrosive fluids derived from pore waters in the sandstones below the carbonate reservoirs and bacterial degradation of oil.

Utilizing high-resolution 3D seismic data, this study aims to characterize the 2D and 3D distribution of post-rift normal faults in the Liuhua area of the PRMB in order to analyze the displacement distribution on the fault planes of different normal faults. Subsequent discussions will focus on how deep the post-rift normal faults cutting through carbonate platforms extend downward, aiming to propose an alternative genetic model for the karst caves to provide a typical example that maybe useful for petroleum development in carbonate oilfields.

2 Geological settings

As one of the largest marginal seas in the western Pacific, the SCS is located at the interaction region of the Eurasian, Indo-Australian, and Philippine Sea Plates (Wang et al., 2023b). It is bordered by the South China Plate in the north, the Ailao Shan-Red River Shear Zone and the East Vietnam Fault in the west, the Palawan and Borneo Islands in the south, and the Manila Subduction Zone in the east (Gao et al., 2019; Sun et al., 2022). Based on bathymetric, gravity, and magnetic surveys, the SCS Basin can be divided into the East Subbasin, Northwest Subbasin, and Southwest Subbasin (Taylor and Hayes, 1983; Briais et al., 1993; Nissen et al., 1995a; Nissen et al., 1995b; Li et al., 2014; Gao et al., 2019). The SCS has experienced multiple tectonic activities, including rifting from the Late Cretaceous to the Oligocene and subsequent seafloor spreading until the early to middle Miocene. Despite still being controversial, the ages of seafloor spreading of the SCS were cited by most authors to start from ~33–34 Ma and to terminate at 15–16 Ma after the IODP 349 Expedition (e.g., Li et al., 2012, 2014, 2015 and 2021; Wu et al., 2014; Lester et al., 2014; Fan et al., 2017; Larsen et al., 2018; Zhang et al., 2018; Gao et al., 2019; Song et al., 2019; Deng et al., 2020; Wang et al., 2023b).

A series of Cenozoic sedimentary basin were formed in the northern passive margin after rifting and seafloor spreading of the SCS, including the Beibuwan Basin, Qiongdongnan Basin, PRMB, and Taixinan Basin (Sun et al., 2009). The PRMB oriented to northeast–southwest has experienced six important tectonic events with the northern SCS (named the Shenhu Event, Zhuqiong Ⅰ Event, Zhuqiong Ⅱ Event, Nanhai Event, Baiyun Event, and Dongsha Event) (Fig. 1a; Gao et al., 2015). It can be divided into secondary tectonic units, including the Northern Fault Terrace, Zhu Ⅰ to Zhu Ⅲ Depressions, Shenhu-Ansha Rise, Panyu Swell, Dongsha Rise, Chaoshan Depression, and Southern Rise (Shi et al., 2005). Our study area is located at the southwestern Dongsha Rise and near the Baiyun Sag (Fig. 1b). The Liuhua 11-1 oilfield, which is the largest offshore oilfield in China, is situated in the study area (Sun et al., 2013). Based on the geological and seismic data, it was believed that three tectonic events occurred in the PRMB before Dongsha Event, namely the Zhuqiong Event, the Nanhai Event and the Baiyun Event (Dong et al., 2009). During this stage, faults emerged along the NE and NEE directions, leading to the formation of a series of anticlines, synclines, and half-grabens (Wang et al., 2021). Subsequently, the NW and NWW-oriented faults, characterized primarily by extension and oblique extension, are developed nearly parallel to the northern margin of the SCS. These faults occurred later than the NE and NEE-oriented faults and are believed to have formed during the Dongsha Event. (Lüdmann and Wong, 1999; Zhao et al., 2012; Chen et al., 2015).

3 Data and methods

This study used high-resolution 3D seismic data covering an area of 813 km^2 with a grid cell size of 18.75 m × 12.5 m and at a water depth of ~300 m in the Liuhua oilfield of the western Dongsha Rise (Fig.1; Wu et al., 2014). The seismic data exhibited a frequency bandwidth of 45–100 Hz with a dominant frequency of 75 Hz (Sun et al., 2013; Wu et al., 2014; Chen et al., 2015). The vertical resolution of this data is around ~8–10 m. Boreholes and log data of LH11-1-1A and LH11-1-2 were used to interpret the sequence stratigraphy (Sun et al., 2013; Wu et al., 2014). Details of the seismic processing flow were unavailable to our study and the seismic data were interpreted on GeoEast 3.0.

Seven seismic reflections have been identified in the Cenozoic sedimentary section of the PRMB (Fig. 2). Among them, Reflector T40 (16.5 Ma) is the top boundary of the Zhujiang Formation that consists of a set of marine carbonate rocks and is one of the primary reservoirs in the study area (Chai, 2014). Reflector T30 (5.5 Ma) is the main post-rift unconformity in the study area after the seafloor spreading and is related to the Dongsha Event (Wu et al., 2014). Between Reflectors T40 and T30, another two seismic reflectors were also identified based on their variable amplitude and frequency seismic facies in the study area (Sun et al., 2013; Chen et al., 2015).

Coherence volumes, 3D visualizations and 3D mesh modeling were performed to characterize the detailed geometry of the post-rift normal faults and sub-circular holes in the study area. Vertical throw values of the horizons were measured on the normal faults using seismic images perpendicular to the fault strike with each of the 10 traces (Fig. 3a). It displayed as T-z plots and contoured fault plane projections following the standard processes outlined by Barnett et al. (1987), Cartwright et al. (1998), and Baudon and Cartwright (2008) (Figs 3b, c, and d).

Previous studies have verified that the T-z plots show very similar overall patterns in both time and depth (Baudon and Cartwright, 2008; Hu et al., 2021). Therefore, to simplify the fault analysis, this study will not convert the vertical throw-in values of two-way travel time (hereafter, TWT) into depth.

Uncertainties of fault throw measurement are related to sampling interval and differential sedimentary compaction between hanging-wall and footwall (Baudon and Cartwright, 2008; Giba et al., 2012; Hu et al., 2021). Baudon and Cartwright (2008) estimated that the maximum errors in the fault throw

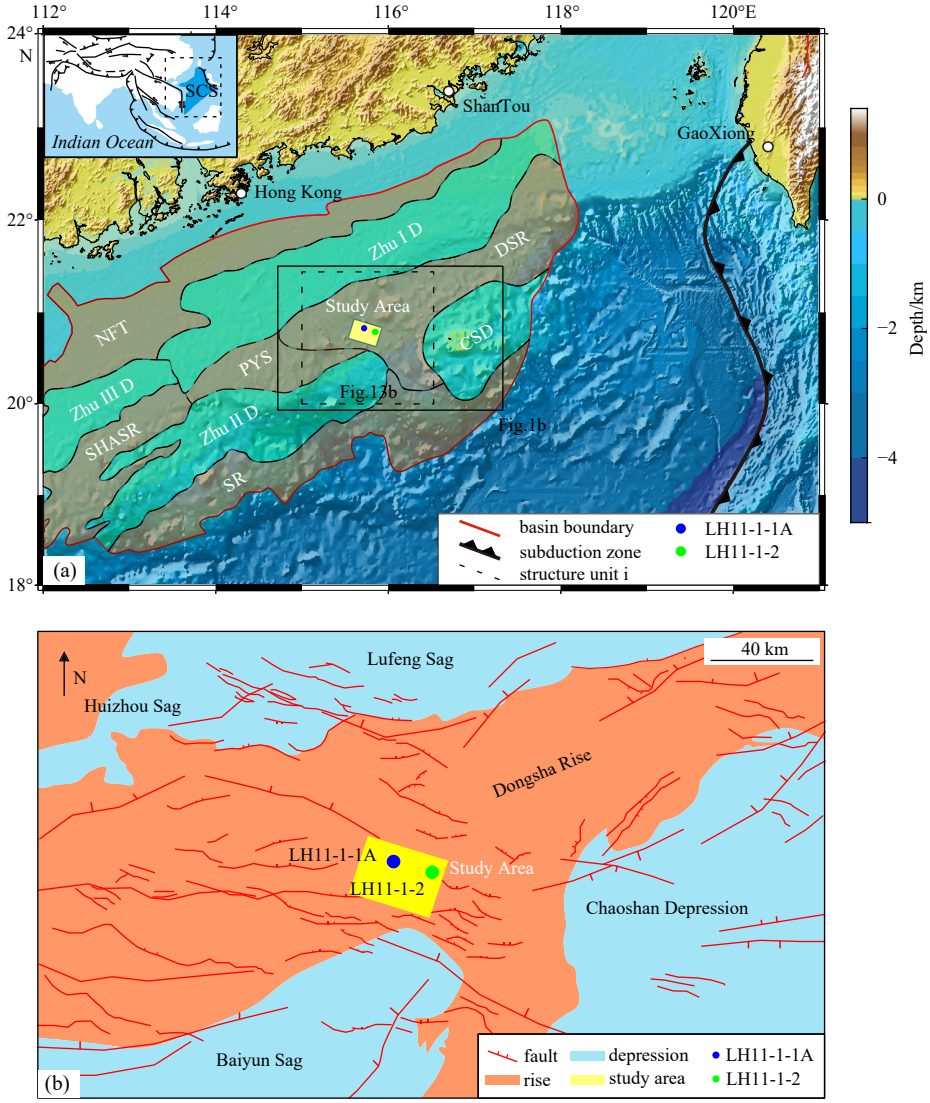

Fig. 1. Structural units in the Pearl River Mouth Basin (modified from Wu et al., 2014) (a); distribution of normal faults around the study area (modified from Li et al., 2004 and Hu, 2016) (b). The yellow area marks the location of the 3D seismic data used in this study. NFT: Northern Fault Terrace; Zhu Ⅰ D : Zhu Ⅰ Depression; Zhu Ⅱ D: Zhu Ⅱ Depression; Zhu Ⅲ D: Zhu Ⅲ Depression; SHASR: Shenhu-Ansha Rise; PYS: Panyu Swell; DSR: Dongsha Rise; CSD: Chaoshan Depression; SR: Southern Rise.

measurement are a fixed value of 2 ms (TWT). The sampling interval determines the accuracy of throw measurements when distinctive and continuous seismic reflections marking and tying the horizons around faults eliminate correlation uncertainties (Baudon and Cartwright, 2008). Inaccuracy due to the differential can be ignored because of small throw values and minor compaction loss (Baudon and Cartwright, 2008; Hu et al., 2021). Fault drag can also lead to throw measurement inaccuracy due to seismic imaging artifacts (Baudon and Cartwright, 2008; Wibberley et al., 2008). Therefore, in this study, throw values were measured at the fault tips with distinctive and continuous seismic reflections and were made at the inflection points closest to the apparent hanging-wall and footwall cut-offs as in previous studies (e.g., Baudon and Cartwright, 2008; Hu et al., 2021).

4 Results

4.1 *General distribution and geometry of post-rift normal faults*

A total of 289 post-rift normal faults were identified in the 3D seismic survey and most are located in the northeastern, central, and southwestern part of the study area (Figs 4a, b). In plan view, these normal faults are mainly oriented NWW-SEE and NW-SE (Figs 4a, b, and c). Among them, about 193, 50, and 23 normal faults are striking N105°–N120°, N130°–N135°, and N90°–N105°, respectively (Fig. 4c). The rest 23 normal faults are oriented to NEE-SWW direction. They consist of complex arrays like horsetail and en-echelon structures (Figs 4a, b).

The longest fault is fault 147, which is located at the central part of the study area and has a length of ~8.4 km in a NWW–SEE direction and with a maximum vertical throw of 38.96 ms (TWT) (Fig. 4a). Fault 279 extending ~7.5 km long has a largest vertical throw of 136 ms (TWT), is oriented to NEE–SWW, and formed a small half-graben-like structure (Figs 4a, d).

In a cross-sectional view, the post-rift normal faults in the Liuhua area are mainly developed in sedimentary layers bounded by Reflectors T30 and T40 (Fig. 4d). The upper-tip lines of many normal faults are located near or below Reflector T30 while others are located at different stratigraphic intervals between Re-

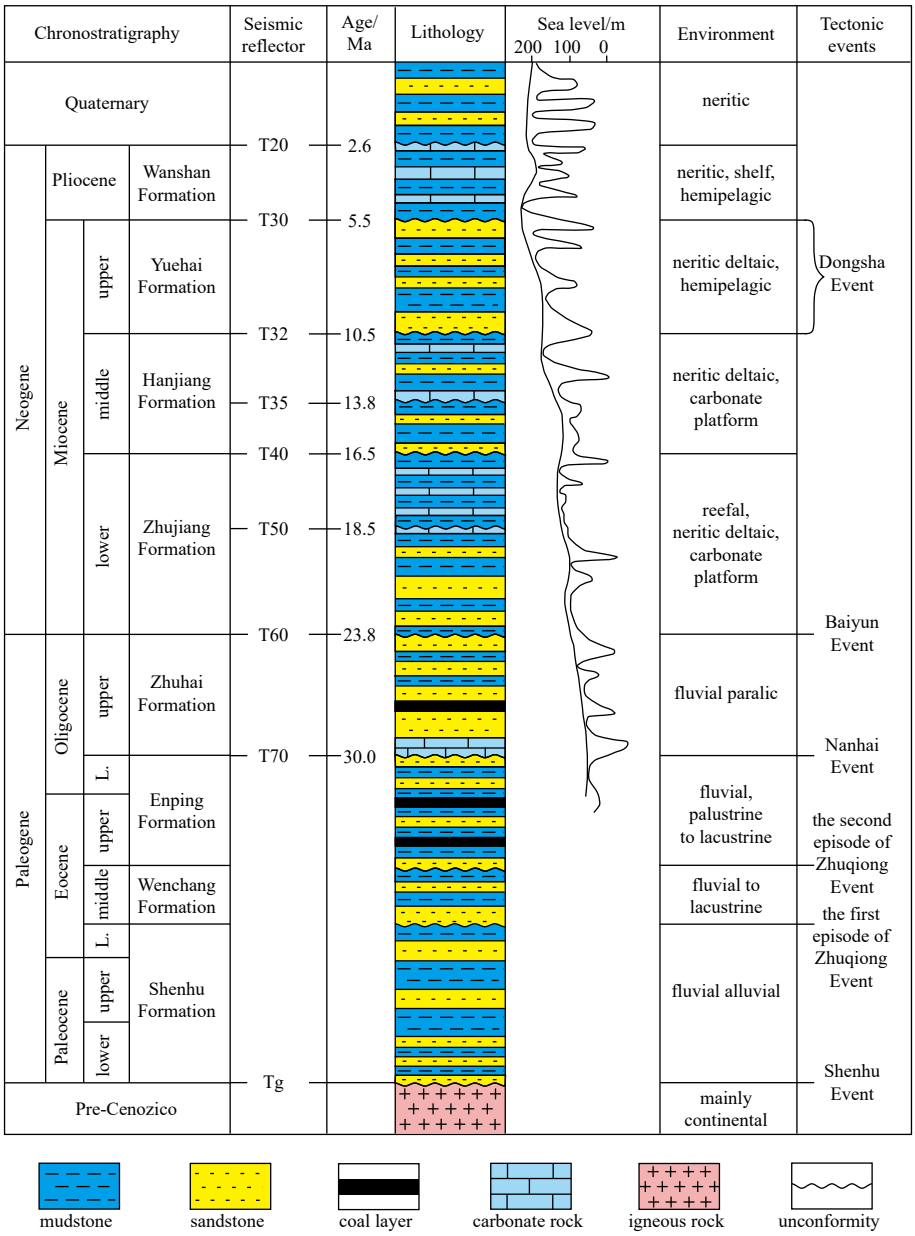

Fig. 2. Cenozoic stratigraphic column with formations, main seismic reflections, and tectonic events of the Pearl River(Zhujiang) Mouth Basin (modified from Wu et al., 2014 and Gao et al., 2015).

flectors T32 and T40. The lower-tip lines are mainly located below Reflectors T35 and T40. Some normal faults extend upward to offset Reflector T30 and downward to cut off Reflector T40 and penetrate into the interior of the carbonate platform. Correspondingly, their upper-tip lines are located above Reflector T30 and lower-tip lines may not be observed due to the chaotic seismic reflections (Figs 4d and 5). Besides, these faults present isolated, "Y"-shaped, "X"-shaped conjugate, and negative flower-like structural combinations that correspond to the horsetail structures in plan view (Figs 4a, b and 5).

4.2 *Detailed geometry and vertical throw analysis of typical normal faults*

According to the faults geometries, vertical throw distributions, and relationship to Liuhua carbonate platform, this study divided the post-rift normal faults into four types: (1) isolated normal faults above the carbonate platform; (2) isolated normal faults cutting through the carbonate platform; (3) conjugate normal faults, and (4) connecting normal faults.

4.2.1 *Isolated normal faults above the carbonate platform (fault 17)*

Fault 17 is located east of the study area, striking the NEE-SWW with a maximum length of 3.38 km (Figs 4a and 6a). Its upper-tips terminate above Reflector T30, and lower-tips are mainly located below Reflector T35 (Fig. 6b). The maximum extension depth reaches –1 219 ms (TWT) at cross-lines 1 410 to 1 420.

Vertical throw distribution plots of fault 17 present relatively flat-topped profiles which are similar to those defined with M-type by Muraoka and Kamata (1983) (Fig. 6c). The throw distribution contours of fault 17 formed a quasi-elliptical shape for the entire fault plane where vertical throw contours largely centred on a maximum throw zone of 9 ms (TWT) (Fig. 6d). A typical feature is that the throw contours on the upper portion are more closely spaced than those on the lower portion (Figs 6c, d). The

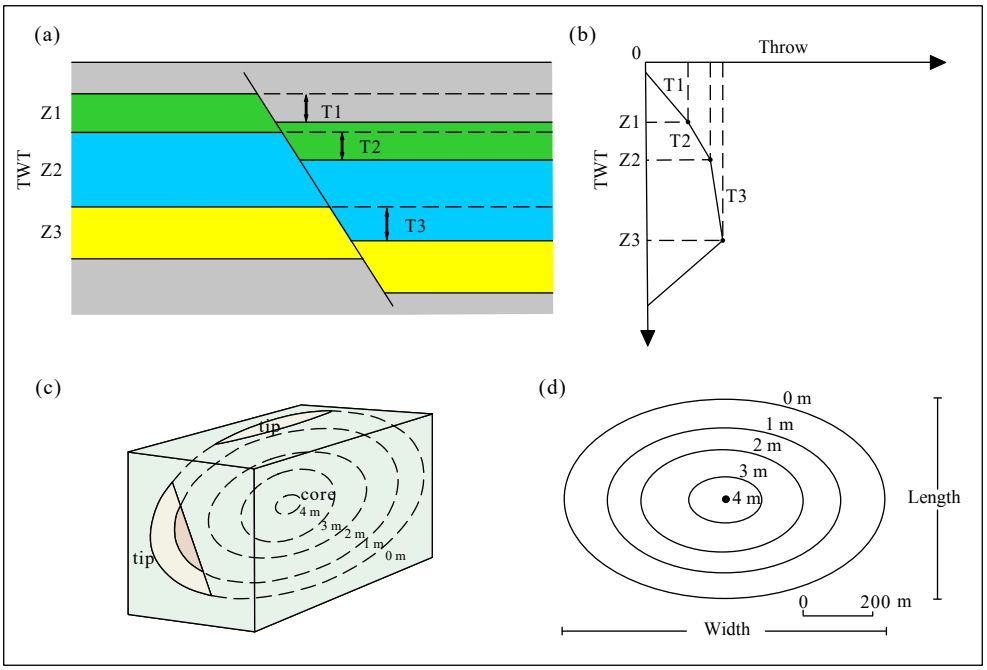

Fig. 3. Geometric aspects of a normal fault. a. Cross section of a normal fault. b. Corresponding T-z plots showing variations of the vertical throw from shallow to deep (modified from Hu et al., 2021). c and d. Ideal elliptical distribution model of a normal fault displaying distribution of vertical throws on the fault plane (modified from Fossen et al., 2016). Z*i* represents the top depth of a sedimentary layer located at the footwall of a normal fault. T*i* represents the vertical throw at each sedimentary layer. The T-z plots show the relationship between Z*i* and T*i*.

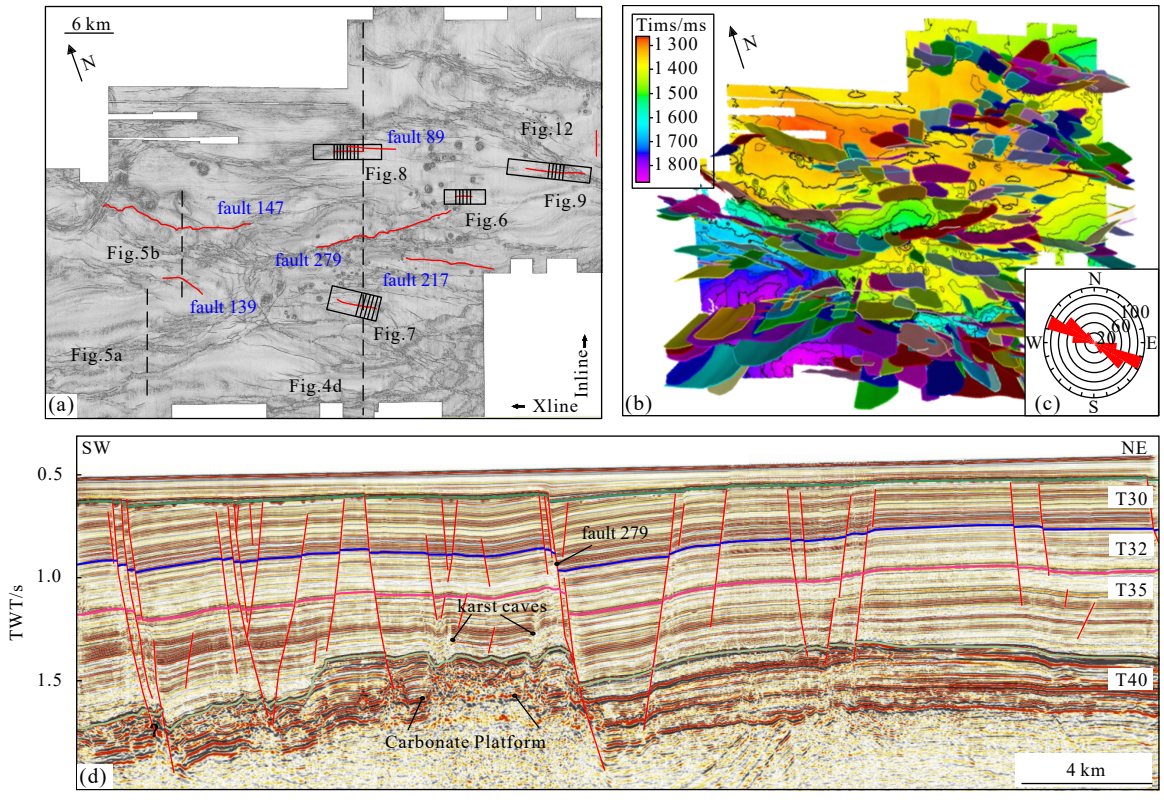

Fig. 4. Coherent variance time-slice at 1 199 ms (TWT) showing that distributions of normal faults and karst caves (a), 3D spatial distribution of post-rift normal faults and the contours of Reflector T40 (b), the rose map showing the predominant NWW–SEE and E–W orientation of the normal faults interpreted in b. c, and d. Interpreted seismic profile crosses the study area highlighting the normal faults, seismic stratigraphic units, and seismic characteristics of carbonate platform.

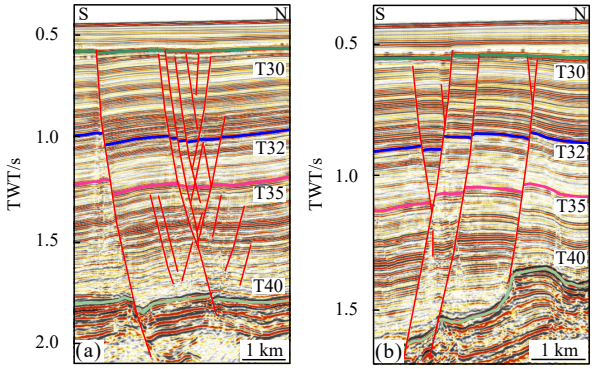

Fig. 5. Seismic profiles exhibiting negative-flower-like structures (a) and "Y"-shaped structures (b).

fault throws increase from 0 ms to 6 ms (TWT) with an average gradient of 0.3 in the upper-tip regions between –561 ms and –581 ms (TWT, 3% of the fault height). In the central section of vertical throw distribution plots (63% of the fault height), little throw variation is observed (Figs 6c, d). The fault throws between –581 ms and –667 ms (TWT, 12% of the fault height) increase from 6 ms to 9 ms (TWT) with an average gradient of 0.034 and they decrease from 9 ms to 6 ms (TWT) with an average gradient of 0.012 between –735 ms and –985 ms (TWT, 39% of the fault height). The lower-tip regions between –985 ms and –1 219 ms (TWT, 35.2% of the fault height) show an average throw gradient of 0.026 with fault throws decreasing from 6 ms (TWT) to 0 ms.

4.2.2 *Isolated normal faults cutting through the carbonate platform (fault 19)*

fault 19 is located south of the study area, striking the NEE-SWW with a maximum length of 2.12 km (Figs 4a and 7a). Its upper-tips terminate below Reflector T30 and its lower-tips are mainly located near Reflector T30 (Fig. 7b). This fault extends downward to the interior of the Liuhua carbonate platform from cross-lines 1 700 to 1 760. The maximum observed fault throw is 19.08 ms (TWT).

Vertical throw distribution plots of fault 19 also show relative flat topped profiles (M-type) (Fig. 7c). Its throw distribution contours exhibit an approximately elliptical shape for the entire fault plane which is similar to that of fault 17 (Figs 6d and 7d). However, the lowermost section of the vertical throw distribution is missing due to the chaotic seismic reflection of the carbonate platform (Figs 7b, c, and d). The core of vertical throw contours is characterized by a maximum throw zone of 12 ms (TWT) (Fig. 7d). In the upper-tip region between –583 ms and –614 ms (TWT, 3% of the fault height), the fault vertical throws in-

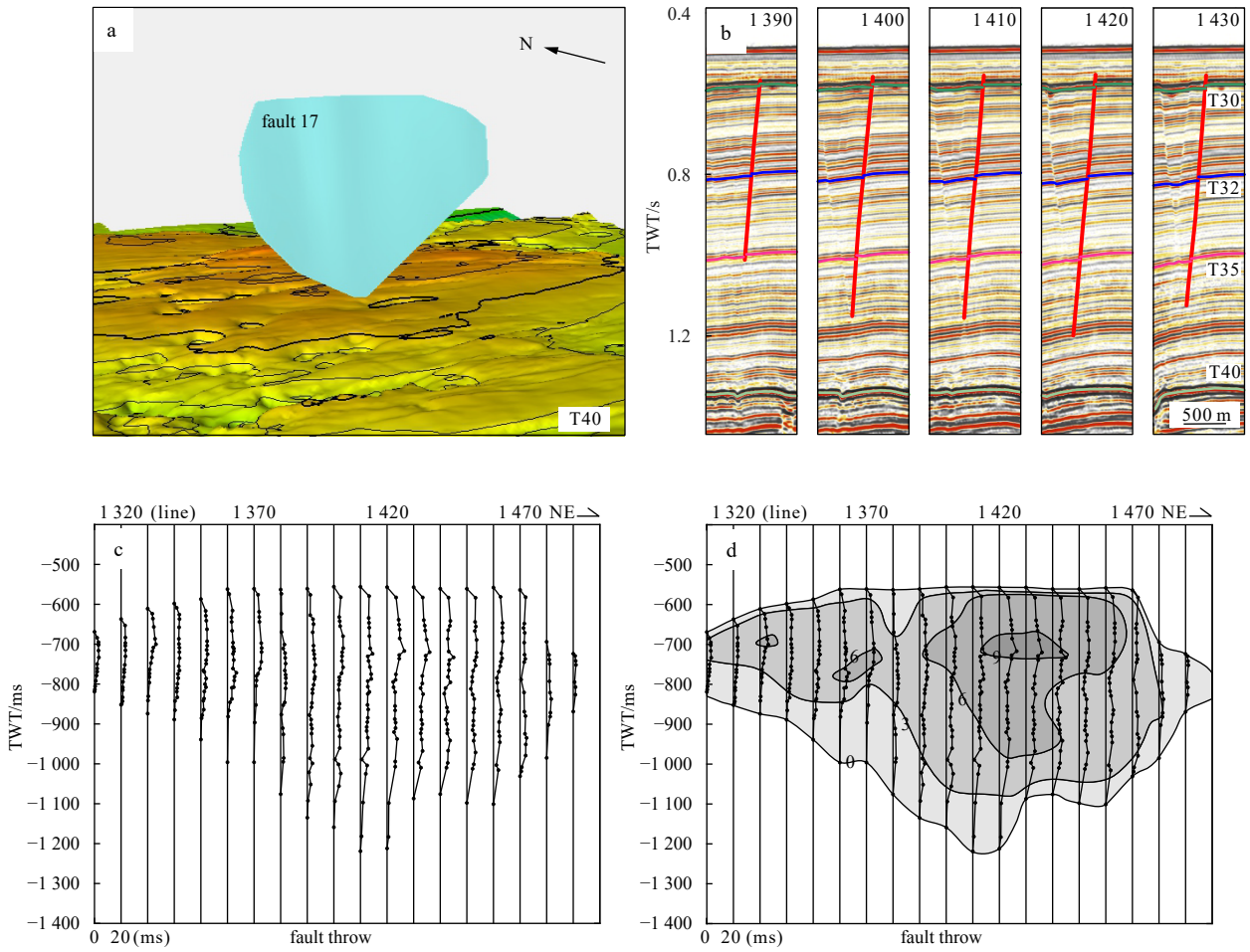

Fig. 6. 3D spatial distribution (a), continuous seismic profiles (b), and throw distribution (c, d) of fault 17. Fig. 6a illustrates relationship between the normal fault and top of carbonate platform. Fig. 6b shows the extended variation of fault 17 from shallow to deep on continuous seismic profiles. Fig. 6c presents the T-z plots every 10 cross-lines. Fig. 6d shows vertical throw contours based on the Fig. 6c. Throw contours are spaced every 3 ms (TWT). Greater displacement values (>9 ms TWT) are indicated as dark colours.

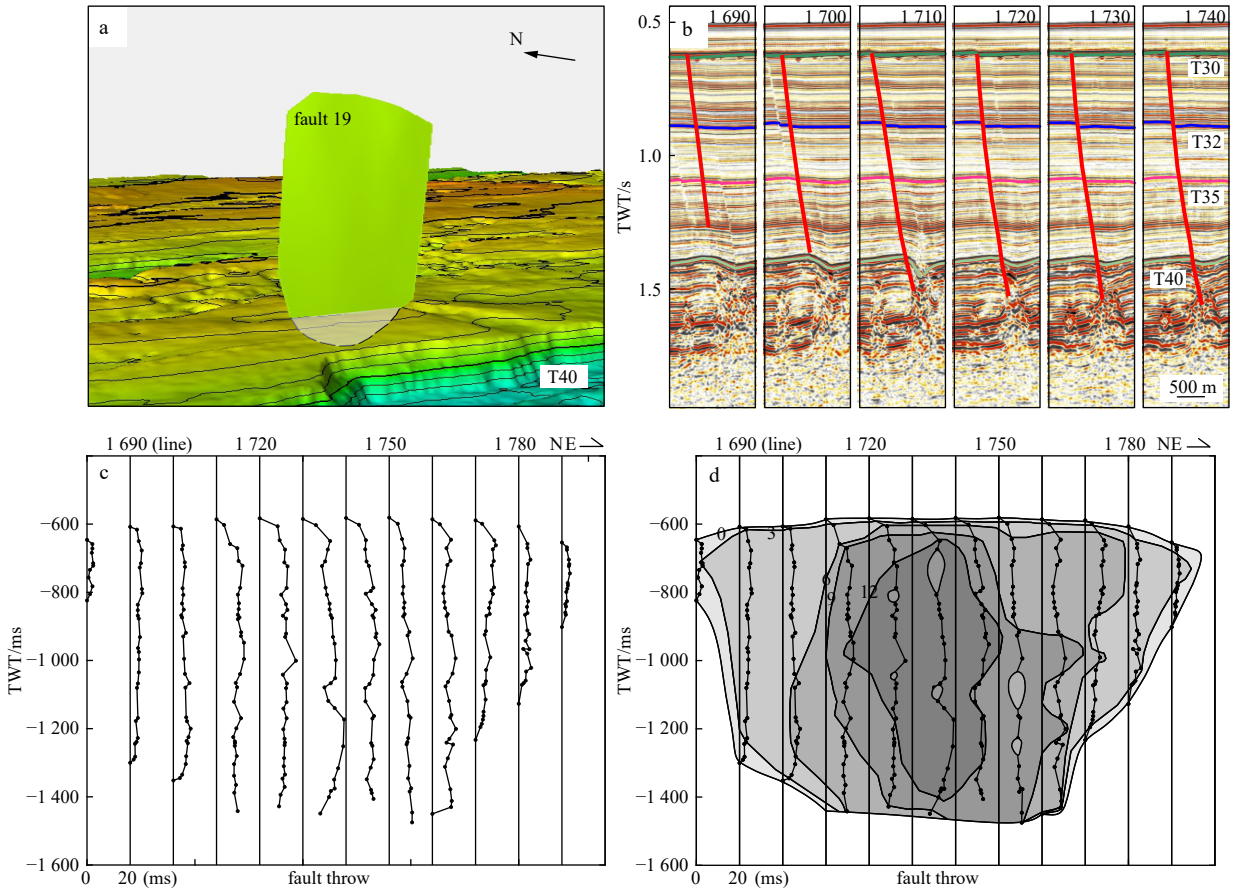

Fig. 7. 3D spatial distribution (a), continuous seismic profiles (b), and throw distribution (c, d) of fault 19. Fig. 7a illustrates relationship between the normal fault and top of carbonate platform. Fig. 7b shows the extended variation of fault 19 from shallow to deep on continuous seismic profiles. Fig. 7c presents the T-z plots every 10 cross-lines. Fig. 7d shows vertical throw contours based on the Fig. 7c. Throw contours are spaced every 3 ms (TWT). Greater displacement values (>12 ms TWT) are indicated as dark colours.

crease from 0 ms to 9 ms with a gradient of 0.19 (Figs 7c, d). In the central section of vertical throw distribution plots (87 % of the fault height), the throw gradient slowly varies from 9 ms to 19 ms (maximum fault throw) with an average value of 0.017 between –614 ms and –1 173 ms (TWT, 65% of the fault height) (Figs 7c, d).

4.2.3 *Conjugate normal fault (fault 276)*

Fault 276 is located northeast of the study area, oriented to the NEE-SWW with a maximum length of 3.18 km and an observed maximum vertical throw of 14.98 ms (TWT) (Figs 4a and 8a). Its upper-tips also terminate below Reflector T30 and its lower-tips are mainly located above Reflector T40. It conjugates another normal fault with opposite dip from cross-lines 1 780 to 1 830 (Fig. 8d).

Vertical throw distribution plots and contours of fault 276 exhibit intense variations on the fault plane (Figs 8b, c). The fault throw abruptly changes to 0 ms in the intersection region of two conjugate faults (Figs 8b, d). The maximum throw zone (9 ms, TWT) is located in the lower section of vertical throw distribution contours on the fault plane (Fig. 8c), which is different from those of faults 17 and 19 described above (Figs 6d and 7d). From cross-lines 1 750 to 1 800, the 6 ms throw contour bends toward the maximum throw zone and the corresponding throw gradient decreases from 0.15 at cross-line 1 760 to 0.017 at cross-line 1 770 (Figs 8b, c). A small concentric ellipse can be observed from –1 169 ms to –1 202 ms (TWT) in depth between cross-lines 1 810 and 1 840. The fault throws in the core is 0 ms, corresponding to the intersection region of two faults. The fault throws of concentric ellipse gradually increase from cross-lines 1 820 to 1 760, which almost dividing the maximum throw zone of 9 ms (TWT) into two sub-zones.

4.2.4 *Connecting normal faults (fault 13)*

Fault 13 is located southeast of the study area, oriented to the E-W with a maximum length of 2.83 km (Figs 4a and 9a). Its upper-tips terminate below Reflector T30 and lower-tips are located at different stratigraphic intervals within the Middle Miocene bounded by Reflectors T32 and T40 (Fig. 9b). The maximum extension depth reaches –1 383 ms (TWT) at cross-lines 1 150 to 1 170.

Vertical throw distribution plots of fault 13 exhibit relatively flat-topped profiles (M-type) (Fig. 9c) like those of fault 17 and 19 (Figs 6c and 7c). Its throw contours exhibit two segments characterized by approximately concentric ellipses and separated by minimal throw a zone of 0 –3 ms (TWT) on the fault plane (Fig. 9d). One segment is located between cross-lines 1 080 and 1 130 (left segment) and the other lies between cross-lines 1 140 and 1 220 (right segment). The former maximum throw zone of 9 ms (TWT) is located at –908 ms to –1 111 ms (TWT) between cross-lines 1 100 and 1 120 while the latter maximum throw zone lies at –774 ms to –1 270 ms (TWT) between cross-lines 1 160 and 1 190, which means that the maximum throw zone region of the

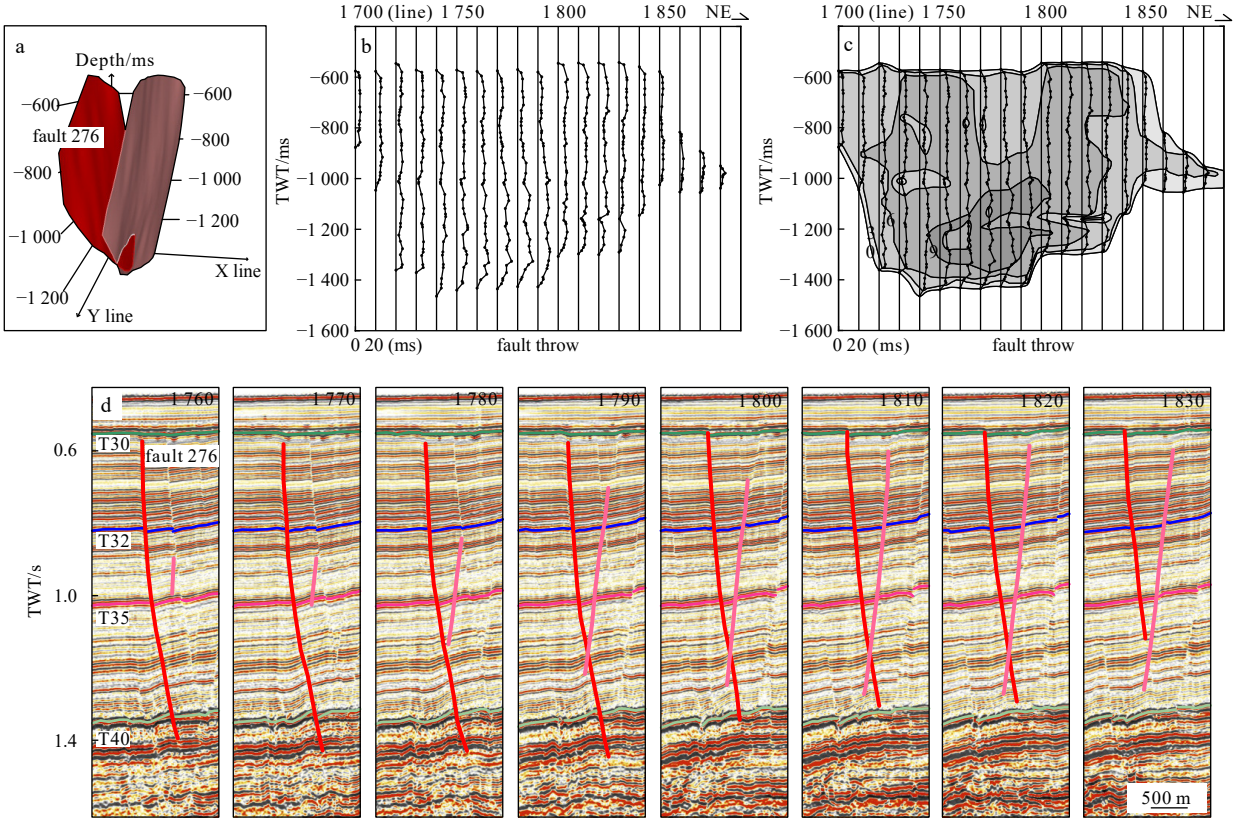

Fig. 8. 3D spatial distribution (a), throw distribution (b, c), and continuous seismic profiles (d) of fault 276. Fig. 8a illustrates fault 276 conjugates with another normal fault. Fig. 8b presents the T-z plots every 10 cross-lines. Fig. 8c shows vertical throw contours based on the Fig. 8b. Fig. 8d shows the extended variation of fault 276 from shallow to deep on continuous seismic profiles. Throw contours are spaced every 3 ms (TWT). Greater displacement values (>9 ms TWT) are indicated as dark colours.

left segment is smaller than that of the right segment.

The fault throws increase from 0 ms to 6 ms (TWT) between -590 ms and –730 ms (TWT, 19% of the fault height) in the upper section of the left segment, displaying an average throw gradient of 0.042. However, the same fault throws variation only occurred in the upper-tips regions between –576 ms and –602 ms (TWT, 3% of the fault height) in the upper section of the right segment (Figs 9c, d), showing an average throw gradient of 0.23. In the central section of vertical throw distribution (6 – 9 ms, TWT), the average throw gradient of the left segment is 0.016 between –730 ms and –908 ms (TWT, 24% of the fault height) while it is 0.023 in the right segment between –683 ms and –811 ms (TWT, 15.9% of the fault height). Towards the lower section of vertical throw distribution, the fault throws decrease from 6 ms to 0–3 ms (TWT) between –1 128 ms and –1 139 ms (TWT) in depth, increase from 0 – 3 ms to 3 ms (TWT) between –1 139 ms and –1 167 ms (TWT), and then decrease to 0 ms at the depth of –1 308 ms (TWT) in the left segment. Correspondingly, the average throw gradient changes from 0.27, to 0.1, and to 0.021. In the right segment, the fault throws decrease from 6 ms (TWT) to 0 ms in lower-tip regions between –1 349 ms and –1 380 ms (TWT, 3% of the fault height) with an average gradient of 0.19.

5 Discussion

5.1 *Extended depth of post-rift normal faults in the interior of the Liuhua carbonate platform*

Our results show that many post-rift normal faults cut off Reflector T40 and extended downward into the Liuhua carbonate platform (Figs 4 and 5). However, the extended depth of these normal faults is difficult to recognize due to the chaotic seismic reflections in the interior of the carbonate platform. This brings challenges and uncertainty in evaluating the qualities and potentialities of the Liuhua carbonate reservoirs. Therefore, based on the symmetric characteristics of the ideal elliptical model of normal fault throw distribution (e.g., Cartwright et al., 1995; Baudon and Cartwright, 2008; Fossen, 2016), this study estimated the extended depth of normal faults that penetrated into the carbonate platform below Reflector T40 to explore whether these normal faults have cut off the entire carbonate reservoir.

We selected four typical post-rift normal faults including fault 19, which cut through the carbonate platform and are located at different regions of the study area (Fig. 4a). Faults 217, 139, and 89 show approximately elliptical shapes for the entire fault planes as the fault 19 (Fig. 10). The fault throw contours of Fault 19 show that the uppermost-tip is at the depth of a –585 ms (TWT) and the core is located at the depth of a –630 ms to –1 149 ms (TWT) (Figs 6d and 10a), indicating that the lowermost-tip of the fault in the carbonate platform was estimated to be from –1 442 ms to –1 569 ms (TWT) (Fig. 10a).

Similarly, the uppermost-tips of faults 217 and 139 are also at –583 ms (TWT) in depth (Figs 10b, c), but their cores are located at depths of –928 ms to –1 259 ms (TWT) and –978 ms to –1 486 ms (TWT), respectively. These mean that the two faults have probably extended downward to –1 380 ms to –1 610 ms (TWT) and –1 714 ms to –1 780 ms (TWT) in the carbonate platform (Figs 10b, c).

The fault throw contours of fault 89 show that the uppermost-

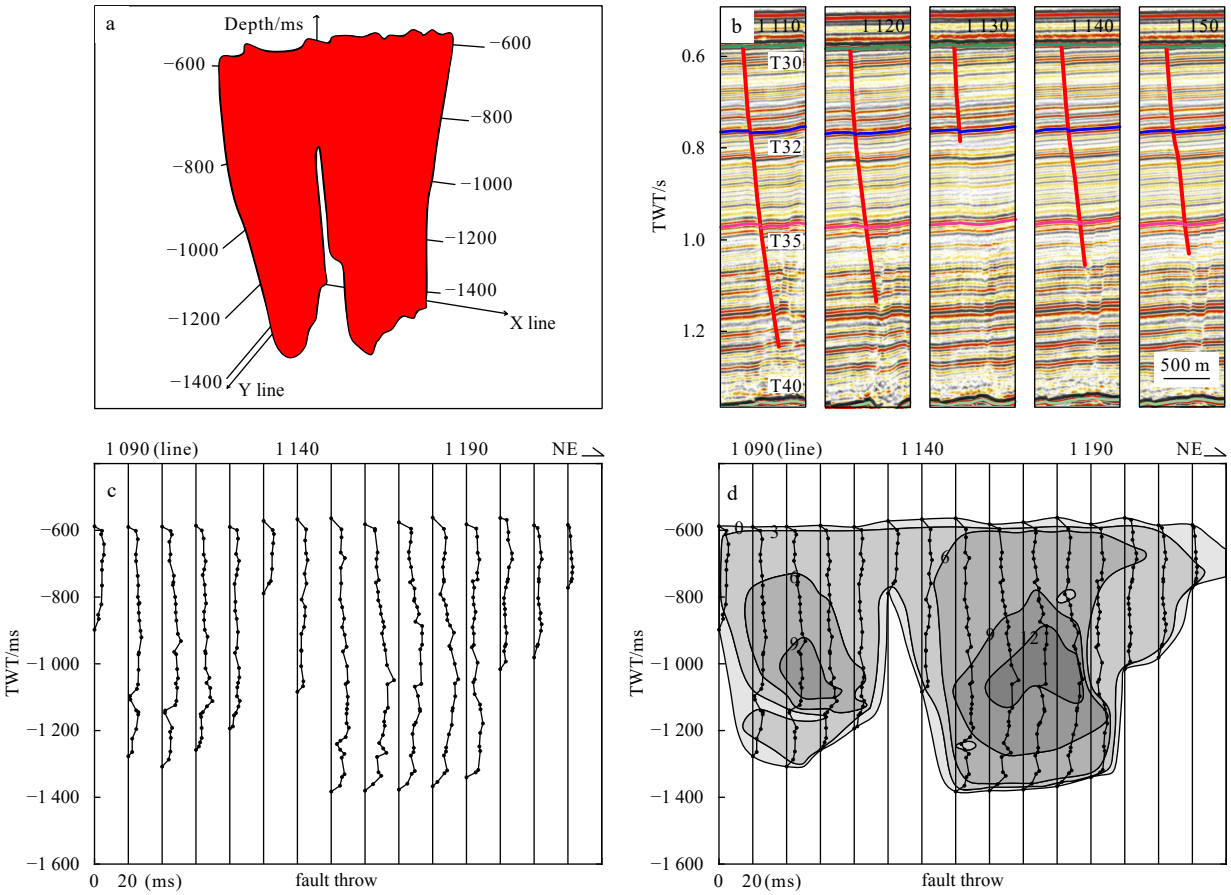

Fig. 9. 3D spatial distribution (a), continuous seismic profiles (b), and throw distribution (c, d) of fault 13. Fig. 9b shows the extended variation of fault 13 from shallow to deep on continuous seismic profiles. Fig. 9c presents the T-z plots every 10 cross-lines. Fig. 9d shows vertical throw contours based on the Fig. 9c, which two maximum throw zones in the central section on the fault plane. Throw contours are spaced every 3 ms (TWT). Greater displacement values (>9 ms TWT) are indicated as dark colours.

tip is located at –581 ms (TWT) and the core lies between –839 ms and –974 ms (TWT) in depth (Fig. 10d), which mean that the lowermost-tip of this fault was estimated to locate between –1 308 ms and –1 410 ms (TWT).

The analysis estimated that the lowermost-tips depth of post-rift normal faults is mainly located between –1 308 ms to –1 780 ms (TWT). Previous seismic profiles calibrated by the Well LH1-1-2 show that Reflector T60 marked the bottom of the Liuhua carbonate platform. This bottom boundary is calculated to be about –1 611 ms to –1 760 ms (TWT) in the study area (Chai, 2014; Chen et al., 2015). Therefore, it seems that these post-rift normal faults may not entirely penetrate through the carbonate platform while they may cause the destruction and redistribution of oil and gas reservoirs in the Liuhua area.

5.2 *Formation mechanisms of karst caves at the top of the Liuhua carbonate platform*

High-resolution 3D seismic data show that abundant karst caves developed at the top of the Liuhua carbonate platform (Figs 4a and 11) and have been described by Sun et al. (2013) and Chen et al. (2015) in detail. These karst caves were suggested to be formed by the dissolution and collapse of the carbonate platform (Sun et al., 2013; Chen et al., 2015), where post-rift normal faults were proposed to serve as pathways for corrosive fluids (Chen et al., 2015). However, our 3D distribution model of post-rift normal faults and amplitude coherence slice show that the distribution extent of these normal faults cutting through the carbonate platform is not well consistent with developed locations of karst caves (Figs 4a, 4b, and 11). Particularly, normal faults are densely distributed in the southwest part of the study area, yet no karst caves have developed. In contrast, karst caves are relatively well-developed in the northwestern part, where only a few normal faults are distributed (Figs 4a and 11).

Additionally, karst cave without normal faults connected has been observed on continuous seismic profiles, which is developed in the interior of the carbonate platform, penetrated through Reflector T40 (top of platform), and continued to extend upward into the middle Miocene strata (Fig. 12). Despite the advantages of the ideal elliptical model for normal fault throw distribution discussed earlier, the post-rift normal faults may lack sufficient depth extension to cut through the carbonate platform completely (Fig. 10) Although the pore water of sandstones was speculated underlying the carbonate reservoirs according to the logging data of wells LH11-1-1A and LH11-1-2 (Zampetti, 2005; Chai, 2014; Chen et al., 2015), There seems to be insufficient evidence to agree that faults can serve as an effective pathway for migrating the deep pore water to form karst caves.

Previous studies showed that oil/gas reservoir was located in the structural highs of our study area (Fig. 13a). The migration direction of oil and gas was from the northwest (Huizhou Sag) and the migration time of oil is inferred to have taken place during the middle-late Miocene (Li, 2010; Chai, 2014; Jiang et al., 2015). The oil and gas accumulation zone, characterized by structural highs, is mainly located in the northeastern part of the

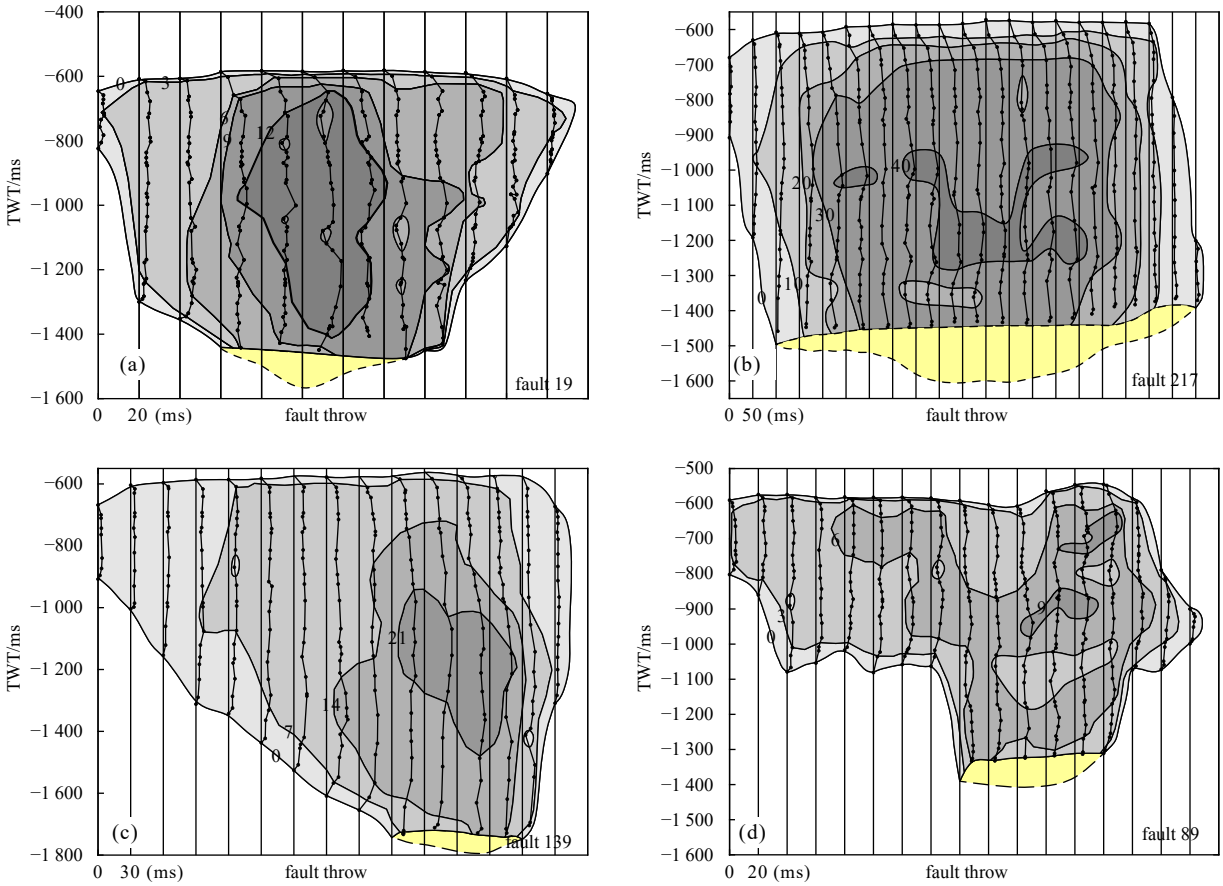

Fig. 10. Measured and estimated fault throw contours of the normal faults 19 (a), 217 (b), 139 (c), and 89 (d) cutting through the carbonate platform. The dark areas mark the maximum throw zones. The yellow areas mark the estimated depth of normal faults.

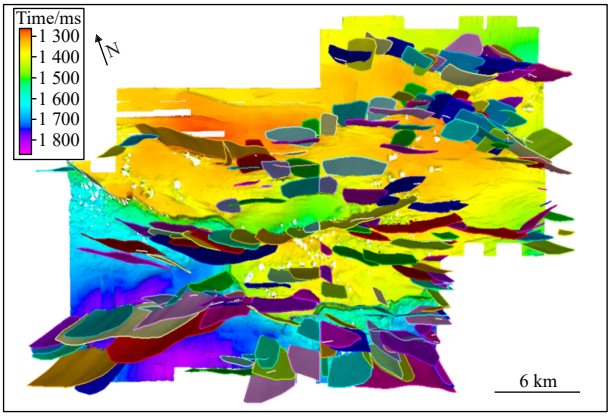

Fig. 11. 3D spatial distribution of normal faults cut off carbonate platform and karst caves. White irregular circles indicate the locations of karst caves.

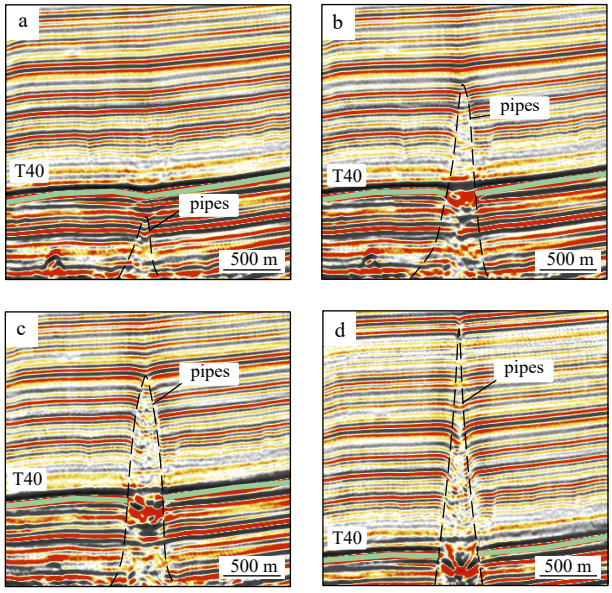

Fig. 12. Continuous seismic profiles illustrate the development of a karst cave with pipe and no normal faults developed.

study area, where only a few karst caves are developed (Fig. 13a). These indicate that the oil and gas accumulation zone is not in good accordance with the distribution of karst caves and carbonic acid corrosion derived from hydrocarbons is not the main factor in the formation of these karst caves.

The formation time of karst caves is mainly in the late Miocene to early Pliocene (Chen et al., 2015), corresponding to the Dongsha Event that had occurred from 10.5 Ma to 5.5 Ma and were characterized by intense faulting re-activation and late Neogene magmatic activities (Lüdmann and Wong, 1999; Wu et al., 2014). In particular, our study area is located at the magmatic belt (Fig. 13b). Previous studies have suggested that large volumes of porosity formed during the burial stages in carbonate reservoirs are believed to result from the mixing corrosion caused by formation fluids and externally sourced fluid at higher temper-

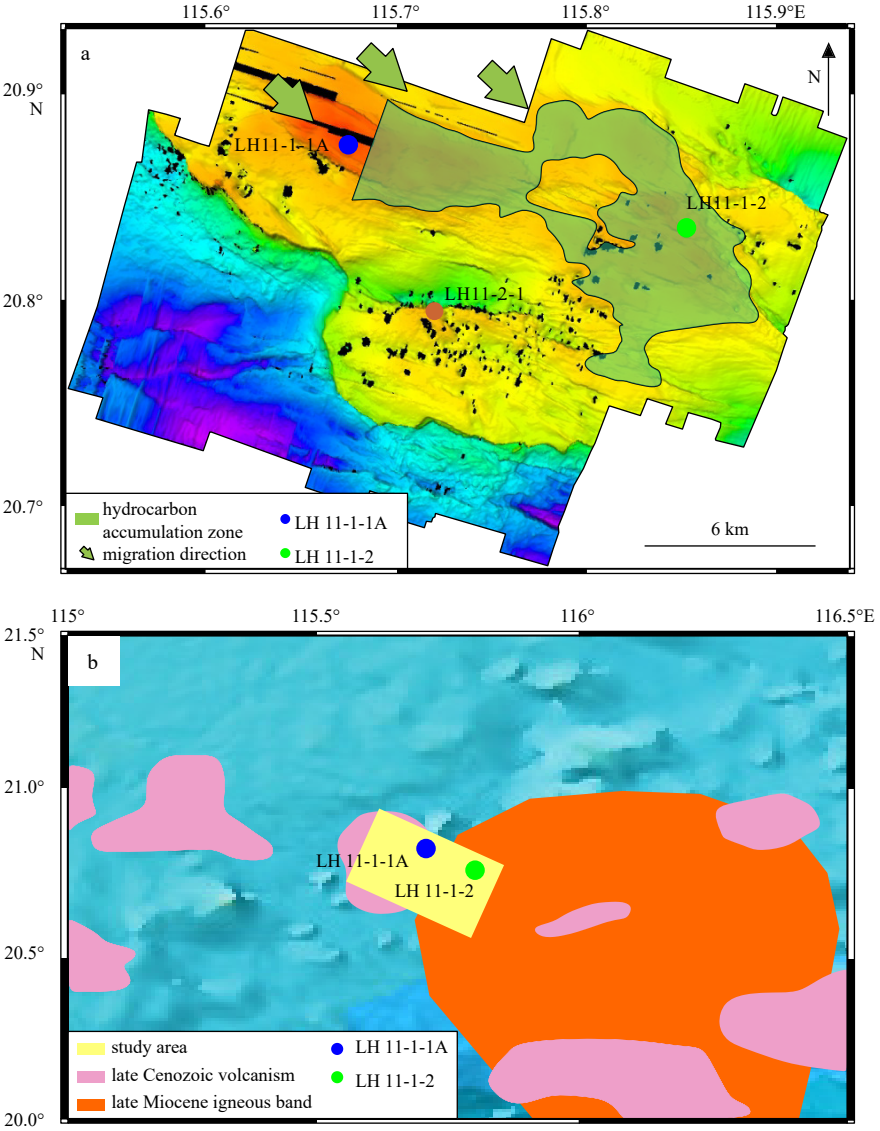

Fig. 13. Distribution (translucent grass green region) of oil and gas accumulation area in the study area (modified from Chai, 2014) (a). Green arrows indicate the migration direction of oil and gas. Extents of late Cenozoic and late Miocene magmatic activities in the Liuhua area (modified from Yan et al., 2006 and Zhao et al., 2021) (b).

atures (Esteban and Taberner, 2003) and one of the more obvious characteristic is the low value of fluid microthermometry $\delta^{18}O$. Sattler (2004) found that the carbonate rocks in the Liuhua area exhibit significantly low values of $\delta^{18}O$ through chemical analysis of the logging curve (LH-11-1-4, LH-11-1-1A, LH-11-1-3) and core materials. Saddle dolomite, which was thought to be a high-temperature product, has been found in the core wafer. The presence of saddle dolomite is believed to be associated with the Miocene volcanic activity in the SCS (Radke and Mathis, 1980; Sattler et al., 2004). In the Liuhua region, it is believed that secondary cavities in the carbonate platform underwent dissolution modification after the compaction process, exhibiting characteristics indicative of later-stage dissolution in deep burial conditions (Hu, 2016). These evidences all support hydrothermal activity at high temperatures in the Liuhua area.

Furthermore, magmatic activities also can generate hydrothermal fluids containing H_2O, CO_2, CO, SO_2, CH_4, and HCl through magma degassing and metamorphic dehydration reactions of sediments surrounding the magma during and after magmatic activities (Westrich and Gerlach, 1992; Villemant and Boudon, 1999; Allard et al., 2005; Hansen, 2006; Aarnes et al., 2010; Iyer et al., 2013; Magee et al., 2017; Gao et al., 2019). These fluids could produce local overpressures to drive themselves upward or flow horizontally (Gao et al., 2019), can be the source of acidic fluids. Therefore, we inferred that magmatic activities occurred in the Dongsha Event produced hydrothermal fluids which provided the main source of the corrosive fluid to form the karst caves in the Liuhua carbonate platform.

In summary, we provide the following scenario to illustrate the formation of karst caves in the Liuhua carbonate platform (Fig. 14). In the middle Miocene, the carbonate platform of Zhujian Formation developed on the sandstone layers of the Zhuhai Formation and the basement blocks was drowned with the rapid sea level rising and was covered by thick mudstones (Fig. 14a; Chen et al., 2015). During the middle-late Miocene, oil and gas formed in the Huizhou Sag migrated from the northwest to the study area and accumulated in the structural highs of the Liuhua carbonate platform (Sun et al., 2013; Jiang et al., 2015). In the late

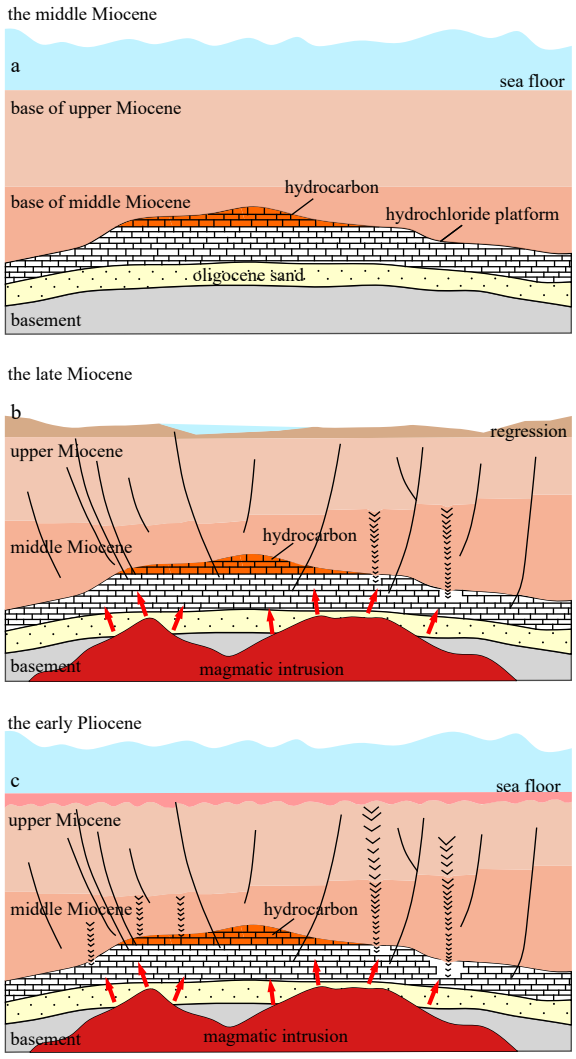

Fig. 14. Schematic formation processes of karst caves in the Zhujiang carbonate platform.

Miocene, the Dongsha Event occurred and caused a series of NWW-trending faults and triggered a large amount of magmatic activities (Fig. 14b). Abundant hydrothermal fluids were released from magma and surrounding heated sediments and accumulated into large volumes to cause over-pressures. These local over-pressures drove the hydrothermal fluids to migrate upward into the carbonate platform and to cause the dissolution and collapse of the carbonate rocks (Fig. 14b). The dissolution and collapse in the carbonate platform continued from the late Miocene to the early Pliocene, which formed a great number of karst caves on the top of platform combing with the oil and gas corrosive fluids (Fig. 14c).

6 Conclusions

This study provided detailed interpretations for the post-rift normal fault in the Liuhua carbonate platform of the PRMB, northern SCS, including geometric shape, spatial distribution, and fault throw distribution. The results indicate the following:

(1) A total of 289 post-rift normal faults were identified in the study area. Theses faults consist of complex arrays like horsetail and en echelon structures that are mainly oriented to NWW–SEE and W-E direction while few of them are in NEE-SWW direction in plan view. They are mainly located between Reflectors T30 and T40 in cross-section view. Some extended upward above Reflector T30 and penetrated downward into the carbonate platform below Reflector T40.

(2) The post-rift normal faults in the study area can be classified into four types: ① isolated normal faults above the carbonate platform; ② isolated normal faults cutting through the carbonate platform; ③ conjugate normal faults, and ④ connecting normal faults. The fault throw contours of the first type present a roughly concentric ellipse with a maximum throw zone on the fault plane. The fault throw distribution on the fault plane of the second type shows similar characteristics to that of the first type but misses the lowermost section because their fault planes are difficult to recognize in the carbonate platform with chaotic seismic reflections. The fault throw contours of the third and fourth types of normal faults do not exhibit classical concentric ellipse as those of the first and second types. The vertical throws of conjugate normal faults anomalously decrease toward their intersection region on the fault plane, whereas the connected normal faults present two maximum vertical throw zones in the central section of the fault plane.

(3) The extended depth of post-rift normal faults cutting through the carbonate platform is estimated from –1 308 ms and –1 780 ms (TWT) using the symmetric elliptical distribution model of fault throw. This means that these normal faults may not penetrate through the entire Liuhua carbonate platform but probably cause the destruction and redistribution of oil and gas reservoirs in the study area.

(4) We proposed that the hydrothermal fluids derived from magmatic activities induced by the Dongsha Event are the main factor in the karst caves at the top of the Liuhua carbonate platform, whereas the oil and gas corrosive fluids play a positive and additional role. The local over-pressures formed the hydrothermal fluids and drove themselves upward into the carbonate platform which caused dissolution and collapse. Our study highlights the dissolution of carbonate reservoirs and the extension of post-rift normal faults should be taken into account considered when assessing the carbonate reservoir heterogeneity and connection in the offshore oilfields with similar characteristics in China and the world.

Acknowledgements

We greatly thank the China National Offshore Oil Company (CNOOC) for their permission to release the data. Those comments are all invaluable and very helpful for revising and improving our paper, as well as in guiding the significance of our research for a wider audience.

References

Aarnes I, Svensen H, Connolly J A D, et al. 2010. How contact metamorphism can trigger global climate changes: modeling gas generation around igneous sills in sedimentary basins. Geochimica et Cosmochimica Acta, 74(24): 7179–7195, doi: 10.1016/j.gca.2010.09.011

Allard P, Burton M, Muré F. 2005. Spectroscopic evidence for a lava fountain driven by previously accumulated magmatic gas. Nature, 433(7024): 407–410, doi: 10.1038/nature03246

Aydin A. 2000. Fractures, faults, and hydrocarbon entrapment, migration and flow. Marine and Petroleum Geology, 17(7): 797–814, doi: 10.1016/S0264-8172(00)00020-9

Barnett J A M, Mortimer J, Rippon J H, et al. 1987. Displacement geometry in the volume containing a single normal fault. AAPG Bulletin, 71(8): 925–937, doi: 10.1306/948878ED-1704-11D7-8645000102C1865D

Baudon C, Cartwright J A. 2008. 3D seismic characterisation of an array of blind normal faults in the Levant Basin, Eastern Mediterranean. Journal of Structural Geology, 30(6): 746–760, doi: 10.

1016/j.jsg.2007.12.008
Briais A, Patriat P, Tapponnier P. 1993. Updated interpretation of magnetic anomalies and seafloor spreading stages in the South China Sea: implications for the Tertiary tectonics of Southeast Asia. Journal of Geophysical Research: Solid Earth, 98(B4): 6299–6328, doi: 10.1029/92JB02280
Cartwright J, Bouroullec R, James D, et al. 1998. Polycyclic motion history of some Gulf Coast growth faults from high-resolution displacement analysis. Geology, 26(9): 819–822, doi: 10.1130/0091-7613(1998)026<0819:PMHOSG>2.3.CO;2
Cartwright J A, Trudgill B D, Mansfield C S. 1995. Fault growth by segment linkage: an explanation for scatter in maximum displacement and trace length data from the Canyonlands Grabens of SE Utah. Journal of Structural Geology, 17(9): 1319–1326, doi: 10.1016/0191-8141(95)00033-A
Chai Nina. 2014. Studies on geochemical characteristics in crude oil and oil -water interface of reef limestone reservoirs-Taking Liuhua l1-1 oilfield of Pearl River Mouth Basin as an example (in Chinese)[dissertation]. Jingzhou: Yangtze University
Chen Duanxin, Wu Shiguo, Völker D, et al. 2015. Tectonically induced, deep-burial paleo-collapses in the Zhujiang Miocene carbonate platform in the northern South China Sea. Marine Geology, 364: 43–52, doi: 10.1016/j.margeo.2015.03.007
Cowie P A, Roberts G P. 2001. Constraining slip rates and spacings for active normal faults. Journal of Structural Geology, 23(12): 1901–1915, doi: 10.1016/S0191-8141(01)00036-0
Davis K, Burbank D W, Fisher D, et al. 2005. Thrust-fault growth and segment linkage in the active Ostler fault zone, New Zealand. Journal of Structural Geology, 27(8): 1528–1546, doi: 10.1016/j.jsg.2005.04.011
Dai Xiangming, Li Zhigang, Sun Chuang, et al. 2022. 3D structural growth and lateral linkage of the normal fault system: a case study from Lufeng sag in the northern South China Sea. Acta Geologica Sinica (in Chinese), 96(6): 1922–1936
Deng Hongdan, Ren Jianye, Pang Xiong, et al. 2020. South China Sea documents the transition from wide continental rift to continental break up. Nature Communications, 11(1): 4583, doi: 10.1038/s41467-020-18448-y
Dong Dongdong, Zhang Gongcheng, Zhong Kai, et al. 2009. Tectonic evolution and dynamics of deepwater area of Pearl River Mouth basin, northern South China Sea. Journal of Earth Science, 20(1): 147–159, doi: 10.1007/s12583-009-0016-1
Esteban M, Taberner C. 2003. Secondary porosity development during late burial in carbonate reservoirs as a result of mixing and/or cooling of brines. Journal of Geochemical Exploration, 78–79: 355–359, doi: 10.1016/S0375-6742(03)00111-0
Faerseth R B, Johnsen E, Sperrevik S. 2007. Methodology for risking fault seal capacity: Implications of fault zone architecture. AAPG Bulletin, 91(9): 1231–1246, doi: 10.1306/03080706051
Fan Chaoyan, Xia Shaohong, Zhao Fang, et al. 2017. New insights into the magmatism in the northern margin of the South China Sea: Spatial features and volume of intraplate seamounts. Geochemistry, Geophysics, Geosystems, 18(6): 2216–2239, doi: 10.1002/2016GC006792
Gao Jinwei, Bangs N, Wu Shiguo, et al. 2019. Post - seafloor spreading magmatism and associated magmatic hydrothermal systems in the Xisha uplift region, northwestern South China Sea. Basin Research, 31(4): 688–708, doi: 10.1111/bre.12338
Gao Jinwei, Wu Shiguo, McIntosh K, et al. 2015. The continent–ocean transition at the mid-northern margin of the South China Sea. Tectonophysics, 654: 1–19, doi: 10.1016/j.tecto.2015.03.003
Giba M, Walsh J J, Nicol A. 2012. Segmentation and growth of an obliquely reactivated normal fault. Journal of Structural Geology, 39: 253–267, doi: 10.1016/j.jsg.2012.01.004
Hansen D M. 2006. The morphology of intrusion - related vent structures and their implications for constraining the timing of intrusive events along the NE Atlantic margin. Journal of the Geological Society, 163(5): 789–800, doi: 10.1144/0016-76492004-167
Hu Run. 2016. The main controlling factors of reservoir forming of Zhujiang formation in Dongsha Uplift, Pear River Mouth Basin (in Chinese)[dissertation]. Chengdu: Chengdu University of Technology
Hu Shouxiang, Alves T M, Omosanya K O, et al. 2021. Geometric and kinematic analysis of normal faults bordering continental shelves: a 3D seismic case study from the northwest South China Sea. Marine and Petroleum Geology, 133: 105263, doi: 10.1016/j.marpetgeo.2021.105263
Huang Ke, Zhong Guangfa, He Min, et al. 2018. Growth and linkage of a complex oblique-slip fault zone in the Pearl River Mouth Basin, northern South China Sea. Journal of Structural Geology, 117: 27–43, doi: 10.1016/j.jsg.2018.09.002
Hull J. 1988. Thickness-displacement relationships for deformation zones. Journal of Structural Geology, 10(4): 431–435, doi: 10.1016/0191-8141(88)90020-X
Iyer K, Rüpke L, Galerne C Y. 2013. Modeling fluid flow in sedimentary basins with sill intrusions: implications for hydrothermal venting and climate change. Geochemistry, Geophysics, Geosystems, 14(12): 5244–5262, doi: 10.1002/2013GC005012
Jackson C A L, Bell R E, Rotevatn A, et al. 2017. Techniques to determine the kinematics of synsedimentary normal faults and implications for fault growth models. Geological Society, London, Special Publications, 439(1): 187–217, doi: 10.1144/SP439.22
Jiang Kaixi, He Wenxiang, Peng Li, et al. 2015. Initial exploration mechanism of dissolution of Zhujiang carbonates by acid fluids under the burial condition in the Liuhua Area of the Pearl River Mouth Basin, South China Sea. Bulletin of Mineralogy, Petrology and Geochemistry (in Chinese), 34(3): 592–600
Kim T W, Park H L, Lee J Y, et al. 1994. Interfacial layer formation of the CdTe/InSb heterointerfaces grown by temperature gradient vapor transport deposition. Applied Physics Letters, 65(20): 2597–2599, doi: 10.1063/1.112579
Kim Y S, Sanderson D J. 2005. The relationship between displacement and length of faults: a review. Earth-Science Reviews, 68(3-4): 317–334, doi: 10.1016/j.earscirev.2004.06.003
Knott S D, Beach A, Brockbank P J, et al. 1996. Spatial and mechanical controls on normal fault populations. Journal of Structural Geology, 18(2-3): 359–372, doi: 10.1016/S0191-8141(96)80056-3
Larsen H C, Mohn G, Nirrengarten M, et al. 2018. Rapid transition from continental breakup to igneous oceanic crust in the South China Sea. Nature Geoscience, 11(10): 782–789, doi: 10.1038/s41561-018-0198-1
Lester R, Van Avendonk H J A, McIntosh K, et al. 2014. Rifting and magmatism in the northeastern South China Sea from wide - angle tomography and seismic reflection imaging. Journal of Geophysical Research: Solid Earth, 119(3): 2305–2323, doi: 10.1002/2013JB010639
Li Hongbo. 2010. The features of construct and structure and the discussion of relationship between evolution with hydrocarbon reservoiring in Huizhou depression and Dongsha Massif of Pearl River Mouth basin (in Chinese)[dissertation]. Wuhan: China University of Geosciences
Li Tingdong, Gen Shufang, Yan Keming, et al. 2004. Asia and Europe Geological Map (1: 5 000 000) (in Chinese). Beijing: Geology Press
Li Yuhan, Huang Haibo, Grevemeyer I, et al. 2021. Crustal structure beneath the Zhongsha Block and the adjacent abyssal basins, South China Sea: new insights into rifting and initiation of seafloor spreading. Gondwana Research, 99: 53–76, doi: 10.1016/j.gr.2021.06.015
Li Chunfeng, Li Jiabiao, Ding Weiwei, et al. 2015. Seismic stratigraphy of the central South China Sea basin and implications for neotectonics. Journal of Geophysical Research: Solid Earth, 120(3): 1377–1399, doi: 10.1002/2014JB011686
Li Chunfeng, Song Taoran. 2012. Magnetic recording of the Cenozoic oceanic crustal accretion and evolution of the South China Sea basin. Chinese Science Bulletin, 57(24): 3165–3181, doi: 10.1007/s11434-012-5063-9
Li Chunfeng, Xu Xing, Lin Jian, et al. 2014. Ages and magnetic structures of the South China Sea constrained by deep tow magnetic surveys and IODP Expedition 349. Geochemistry, Geophysics,

Geosystems, 15(12): 4958–4983, doi: 10.1002/2014GC005567
Lüdmann T, Wong H K. 1999. Neotectonic regime on the passive continental margin of the northern South China Sea. Tectonophysics, 311(1–4): 113–138, doi: 10.1016/S0040-1951(99)00155-9
Magee C, Jackson C A L, Hardman J P, et al. 2017. Decoding sill emplacement and forced fold growth in the Exmouth Sub-basin, offshore northwest Australia: implications for hydrocarbon exploration. Interpretation, 5(3): SK11–SK22, doi: 10.1190/INT-2016-0133.1
Muraoka H, Kamata H. 1983. Displacement distribution along minor fault traces. Journal of Structural Geology, 5(5): 483–495, doi: 10.1016/0191-8141(83)90054-8
Nicol A, Childs C, Walsh J J, et al. 2017. Interactions and growth of faults in an outcrop-scale system. Geological Society, London, Special Publications, 439(1): 23–39, doi: 10.1144/SP439.9
Nissen S S, Hayes D E, Bochu Y, et al. 1995a. Gravity, heat flow, and seismic constraints on the processes of crustal extension: northern margin of the South China Sea. Journal of Geophysical Research: Solid Earth, 100(B11): 22447–22483, doi: 10.1029/95jb01868
Nissen S S, Hayes D E, Buhl P, et al. 1995b. Deep penetration seismic soundings across the northern margin of the South China Sea. Journal of Geophysical Research: Solid Earth, 100(B11): 22407–22433, doi: 10.1029/95JB01866
Palumbo L, Benedetti L, Bourlès D, et al. 2004. Slip history of the Magnola fault (Apennines, Central Italy) from ^{36}Cl surface exposure dating: evidence for strong earthquakes over the Holocene. Earth and Planetary Science Letters, 225(1-2): 163–176, doi: 10.1016/j.epsl.2004.06.012
Peacock D C P, Sanderson D J. 1991. Displacements, segment linkage and relay ramps in normal fault zones. Journal of Structural Geology, 13(6): 721–733, doi: 10.1016/0191-8141(91)90033-F
Radke B M, Mathis R L. 1980. On the formation and occurrence of saddle dolomite. Journal of Sedimentary Research, 50(4): 1149–1168, doi: 10.1306/212F7B9E-2B24-11D7-8648000102C1865D
Rippon J H. 1984. Contoured patterns of the throw and hade of normal faults in the Coal Measures (Westphalian) of north-east Derbyshire. Proceedings of the Yorkshire Geological Society, 45(3): 147–161, doi: 10.1144/pygs.45.3.147
Roberts G P, Michetti A M. 2004. Spatial and temporal variations in growth rates along active normal fault systems: an example from The Lazio–Abruzzo Apennines, central Italy. Journal of Structural Geology, 26(2): 339–376, doi: 10.1016/S0191-8141(03)00103-2
Rotevatn A, Jackson C A L, Tvedt A B M, et al. 2019. How do normal faults grow? Journal of Structural Geology, 125: 174–184, doi: 10.1016/J.JSG.2018.08.005
Sattler U, Zampetti V, Schlager W, et al. 2004. Late leaching under deep burial conditions: a case study from the Miocene Zhujiang Carbonate Reservoir, South China Sea. Marine and Petroleum Geology, 21(8): 977–992, doi: 10.1016/j.marpetgeo.2004.05.005
Shi Xiaobin, Burov E, Leroy S, et al. 2005. Intrusion and its implication for subsidence: a case from the Baiyun Sag, on the northern margin of the South China Sea. Tectonophysics, 407(1–2): 117–134, doi: 10.1016/j.tecto.2005.07.004
Shipton Z K, Cowie P A. 2001. Damage zone and slip-surface evolution over μm to km scales in high-porosity Navajo sandstone, Utah. Journal of Structural Geology, 23(12): 1825–1844, doi: 10.1016/S0191-8141(01)00035-9
Song Taoran, Li Chunfeng, Wu Shiguo, et al. 2019. Extensional styles of the conjugate rifted margins of the South China Sea. Journal of Asian Earth Sciences, 177: 117–128, doi: 10.1016/j.jseaes.2019.03.008
Song Xianqiang, Wang Haixue, Fu Xiaofei, et al. 2022. Hydrocarbon retention and leakage in traps bounded by active faults: A case study from traps along the NDG fault in the Qinan area, Bohai Bay Basin, China. Journal of Petroleum Science and Engineering, 208: 109344, doi: 10.1016/j.petrol.2021.109344
Sun Qiliang, Cartwright J, Wu Shiguo, et al. 2013. 3D seismic interpretation of dissolution pipes in the South China Sea: genesis by subsurface, fluid induced collapse. Marine Geology, 337: 171–181, doi: 10.1016/j.margeo.2013.03.002
Sun Qiliang, Wang Qing, Shi Fengyan, et al. 2022. Runup of landslide-generated tsunamis controlled by paleogeography and sea-level change. Communications Earth & Environment, 3(1): 244, doi: 10.1038/s43247-022-00572-w
Sun Zhen, Zhong Zhihong, Keep M, et al. 2009. 3D analogue modeling of the South China Sea: a discussion on breakup pattern. Journal of Asian Earth Sciences, 34(4): 544–556, doi: 10.1016/j.jseaes.2008.09.002
Taylor B, Hayes D E. 1983. Origin and history of the South China Sea basin. In: Hayes D E. The Tectonic and Geologic Evolution of Southeast Asian Seas and Islands: Part 2. Washington: American Geophysical Union, 23–56, doi: 10.1029/GM027
Trudgill B, Cartwright J. 1994. Relay-ramp forms and normal-fault linkages, Canyonlands National Park, Utah. GSA Bulletin, 106(9): 1143–1157, doi: 10.1130/0016-7606(1994)106<1143:RRFANF>2.3.CO;2
Villemant B, Boudon G. 1999. H_2O and halogen (F, Cl, Br) behaviour during shallow magma degassing processes. Earth and Planetary Science Letters, 168(3–4): 271–286., doi: 10.1016/S0012-821X(99)00058-8
Walsh J J, Bailey W R, Childs C, et al. 2003. Formation of segmented normal faults: a 3-D perspective. Journal of Structural Geology, 25(8): 1251–1262, doi: 10.1016/S0191-8141(02)00161-X
Walsh J J, Watterson J. 1987. Distributions of cumulative displacement and seismic slip on a single normal fault surface. Journal of Structural Geology, 9(8): 1039–1046, doi: 10.1016/0191-8141(87)90012-5
Walsh J J, Watterson J. 1988. Analysis of the relationship between displacements and dimensions of faults. Journal of Structural Geology, 10(3): 239–247, doi: 10.1016/0191-8141(88)90057-0
Walsh J J, Watterson J. 1989. Displacement gradients on fault surfaces. Journal of Structural Geology, 11(3): 307–316, doi: 10.1016/0191-8141(89)90070-9
Wang Xingxing, Kneller B, Sun Qiliang. 2023a. Sediment waves control origins of submarine canyons. Geology, 51(3): 310–314, doi: 10.1130/G50642.1
Wang Pengcheng, Li Sanzhong, Suo Yanhui, et al. 2021. Structural and kinematic analysis of Cenozoic rift basins in South China Sea: a synthesis. Earth-Science Reviews, 216: 103522, doi: 10.1016/j.earscirev.2021.103522
Wang Qiang, Zhao Minghui, Zhang Jiazheng, et al. 2023b. Breakup mechanism of the northern South China Sea: evidence from the deep crustal structure across the continent-ocean transition. Gondwana Research, 120: 47–69, doi: 10.1016/j.gr.2022.09.004
Watterson J. 1986. Fault dimensions, displacements and growth. Pure and Applied Geophysics, 124(1–2): 365–373, doi: 10.1007/BF00875732
Westrich H R, Gerlach T M. 1992. Magmatic gas source for the stratospheric SO_2 cloud from the June 15, 1991, eruption of Mount Pinatubo. Geology, 20(10): 867–870, doi: 10.1130/0091-7613(1992)020<0867:MGSFTS>2.3.CO;2
Wibberley C A J, Yielding G, Di Toro G. 2008. Recent advances in the understanding of fault zone internal structure: a review. Geological Society, London, Special Publications, 299(1): 5–33, doi: 10.1144/SP299.2
Willemse E J M, Pollard D D, Aydin A. 1996. Three-dimensional analyses of slip distributions on normal fault arrays with consequences for fault scaling. Journal of Structural Geology, 18(2-3): 295–309, doi: 10.1016/S0191-8141(96)80051-4
Wu Shiguo, Gao Jinwei, Zhao Shujuan, et al. 2014. Post-rift uplift and focused fluid flow in the passive margin of northern South China Sea. Tectonophysics, 615–616: 27–39, doi: 10.1016/j.tecto.2013.12.013
Yan Pin, Deng Hui, Liu Hailing, et al. 2006. The temporal and spatial distribution of volcanism in the South China Sea region. Journal of Asian Earth Sciences, 27(5): 647–659, doi: 10.1016/j.jseaes.2005.06.005
Zampetti V, Sattler U, Braaksma H. 2005. Well log and seismic character of Liuhua 11-1 Field, South China Sea; relationship

between diagenesis and seismic reflections. Sedimentary Geology, 175(1–4): 217–236, doi: 10.1016/j.sedgeo.2004.12.018

Zhang Guoliang, Luo Qing, Zhao Jian, et al. 2018. Geochemical nature of sub-ridge mantle and opening dynamics of the South China Sea. Earth and Planetary Science Letters, 489: 145–155, doi: 10.1016/j.epsl.2018.02.040

Zhao Fang, Berndt C, Alves T M, et al. 2021. Widespread hydrothermal vents and associated volcanism record prolonged Cenozoic magmatism in the South China Sea. GSA Bulletin, 133(11–12): 2645–2660, doi: 10.1130/B35897.1

Zhao Shujuan, Wu Shiguo, Shi Hesheng, et al. 2012. Structures and dynamic mechanism related to the Dongsha movement at the northern margin of South China Sea. Progress in Geophysics (in Chinese), 27(3): 1008–1019, doi: 10.6038/j.issn.1004-2903.2012.03.022